Dalton Transactions

ROYAL SOCIETY OF CHEMISTRY

PAPER

View Article Online
View Journal | View Issue

Cite this: *Dalton Trans.*, 2025, **54**, 8979

Novel curcumin@HKUST-1 composite with enhanced visible light harvesting capacities for photocatalytic applications†

Luis A. Alfonso-Herrera, ‡[a] Jesús S. Rodríguez-Girón, ‡§[a] J. Edgar Carrera-Crespo,[b] Francisco Tzompantzi,[b] Daniel Sánchez-Martínez,[c] Alejandra M. Navarrete-López *[a] and Hiram I. Beltrán *[a]

Received 8th March 2025,
Accepted 5th May 2025

DOI: 10.1039/d5dt00564g

rsc.li/dalton

The **HKUST-1** and related MOFs have been proposed as photocatalysts, nevertheless they presented certain limitations, *e.g.* poor visible light absorption. Thus, we propose the encapsulation of the photosensitizer curcumin (**Cur**) in **HKUST-1** as a strategy to improve light absorption in the resultant **Cur@HKUST-1** composite. The **Cur@HKUST-1** was characterized by XRD, FTIR, TGA, UV-Vis, BET, SEM, and electrochemical experiments confirming the **Cur** infiltration in 2.5%, preserving crystalline structure of **HKUST-1**. DFT calculations for **Cur@HKUST-1** in periodic boundary conditions were employed to elucidate the chemical structure, corroborating experimental evidence. Chronoamperometry experiments in dark and visible light irradiation showed 48% photocurrent density enhancement for **Cur@HKUST-1** *vs.* **HKUST-1**, corroborating the sensitization effect derived from **Cur** inclusion. As a result, **Cur@HKUST-1**, presented 1.2 times (20% higher) photocatalytic hydrogen evolution than free **HKUST-1** under visible light irradiation, just by 2.5% **Cur** loading into the **HKUST-1**, demonstrating infiltration as a suitable, nonlinear, strategy to produce active MOFs for photocatalytic purposes.

1. Introduction

The metal–organic framework (MOF) **HKUST-1** has been employed recently as both a precursor and active component[1–4] of photocatalytic materials aimed to solve a wide variety of key issues that face our modern society. Among these issues are the production of clean hydrogen to replace the pollutant fossil fuels, the removal of pollutants from water sources, the degradation/adsorption of sulfur-based compounds in petroleum refining, or sensing important biomarkers such as L-Cys.[4–8] Nevertheless, bare **HKUST-1** presented limited photocatalytic activity compared to other MOFs. A possible explanation for this fact is that **HKUST-1** contains the trimesic acid (TMA or BTC) linker, which not only is electron-deficient, but also has a small conjugated system, all this provoking a wide bandgap larger than 3 eV in the material, banning visible light harvesting.[4] A clever modification to this material to enhance light absorption properties is coupling **HKUST-1** with sensitizer compounds. A common characteristic of sensitizer compounds is the presence of a large conjugated π-system (*e.g.*, dyes or pigments) promoting light absorption in the UV and the visible region of the electromagnetic spectra.[9] In the sensitization process, the sensitizer harvests the light in the desirable wavelength or even a spectral wavelength range, promoting electron transference from HOMO to LUMO. Afterward, the electrons in the sensitizer LUMO orbital are able to migrate to the conduction band (CB) of the photocatalyst.[9] In this context, curcumin (**Cur**) is an interesting eco-friendly biosensitizer since **Cur** is a cheap and non-toxic molecule with a large conjugated system that confers its photoactivity under the visible region of the electromagnetic spectra.[10] Additionally, it has been reported that the LUMO orbital of **Cur** is higher in energy (−2.765 eV[10]) than the CB of **HKUST-1** (−3.61 eV),[4] which could promote the charge transfer.[10] In the same way, several authors have successfully employed **Cur** to enhance the photocatalytic activity of different systems. For example, in 2017 Lim *et al.*, anchored

[a]*Departamento de Ciencias Básicas, DCBI, Universidad Autónoma Metropolitana, Unidad Azcapotzalco, Av. San Pablo 420, Col. Nueva Rosario, Alc. Azcapotzalco, 02128 CDMX, Mexico. E-mail: amnl@azcu.uam.mx, hibc@azc.uam.mx*
[b]*Departamento de Química, DCBI, Universidad Autónoma Metropolitana, Unidad Iztapalapa, Av. San Rafael Atlixco 186, Col. Leyes de Reforma 1ra Secc, Alc. Iztapalapa, 09340 CDMX, Mexico*
[c]*Departamento de Ecomateriales y Energía, Facultad de Ingeniería Civil, Universidad Autónoma de Nuevo León, UANL, Av. Universidad S/N Ciudad Universitaria, 64455 San Nicolás de Los Garza, Nuevo León, Mexico*

†Electronic supplementary information (ESI) available. See DOI: https://doi.org/10.1039/d5dt00564g

‡These authors contributed equally to this research.

§Posdoctoral position from SECIHTI.

Cur to TiO_2 creating the **Cur@TiO$_2$** composites with enhanced photocatalytic activity toward the degradation of organic compounds, the reduction of chromate, Cr^{VI}, and the generation of OH radicals and H_2O_2 through the reduction of O_2 under visible light (λ > 420 nm). The **Cur@TiO$_2$** composites developed a higher photocurrent compared with the pristine TiO_2, demonstrating the effectiveness of **Cur** for both light harvesting and photocatalytic activity enhancements.[11] On the other hand, in 2015, Kushwaha *et al.*, coupled **Cur** with $Bi_{0.5}Na_{0.5}TiO_3$ perovskite creating the **Cur@Bi$_{0.5}$Na$_{0.5}$TiO$_3$** composite, which was evaluated toward the decolorization of rhodamine 6G (Rh6G). The authors confirmed the sensitization effect of **Cur** through an increment in the absorbance of composites in the 300–800 nm region, in comparison to the pristine material. As a result, the **Cur@Bi$_{0.5}$Na$_{0.5}$TiO$_3$** composite generated an 8-fold decolorization capacity of rhodamine 6G (Rh6G) in comparison to the pristine material. They explained the higher photocatalytic activity by a **Cur → Bi$_{0.5}$Na$_{0.5}$TiO$_3$** charge transfer mechanism involving the movement of electrons from the LUMO of **Cur** to the CB of $Bi_{0.5}Na_{0.5}TiO_3$.[12] Finally, in 2020, Yan *et al.*, developed SiO_2, TiO_2 and **Cur** nanocomposites (**Cur@SiO$_2$/TiO$_2$**). The authors evaluated the pristine materials and the **Cur@SiO$_2$/TiO$_2$** composite toward the reduction of Cr^{IV} under visible light irradiation. The authors confirmed the sensitization effect of **Cur** by an increment in the absorbance of the **Cur@SiO$_2$/TiO$_2$** in the region between 400–600 nm. The previously photo-inactive SiO_2/TiO_2 material, due to the photo-sensitization as the **Cur@SiO$_2$/TiO$_2$** composite, reached a photocatalytic reduction of 100% for Cr^{IV} after 2.5 h of reaction.[13]

In addition, **Cur**-based MOFs have shown a promising photocatalytic activity. That is the case of the work presented by Khandan *et al.*, in 2018, whose synthesized a uranyl–curcumin–MOF (**U-Cur**) employing ultrasound (US), reflux (⇓), hydrothermal (HT) and ultrasound assisted reflux (⇓-US) reaction methodologies. The authors observed that the material synthesized through the ultrasound methodology (**U-Cur$_{US}$**) showed the best physicochemical properties, which led to a high photocatalytic activity toward the degradation of phenol red (99%) after 11 min under UV irradiation.[14]

On the other hand, several authors have demonstrated that the infiltration of **Cur** into **HKUST-1** is feasible; nevertheless, most of these reports have focused on the development of drug carrier systems, missing or overpassing the effect of **Cur** on optical properties while is included in **HKUST-1**. For example, in 2022, Yang *et al.*, employed **Cur@HKUST-1** composites as treatment for diabetic foot ulcers. The authors achieved the infiltration of **Cur** into **HKUST-1** using a post-synthetic methodology from a DMSO–**Cur** solution (100 mg mL^{-1}), obtaining an infiltration degree of 38.35 ± 1.18%. The authors also suggested that the infiltration occurred through π–π interactions and coordination bonds between the guest molecule and the open metal sites of the host.[15] Also in 2022, Tian *et al.*, developed **Cur@HKUST-1@PVP** (PVP = polyvinylpirrolidone) composites for imaging-guided photoacoustics, and as an active material for photothermal therapy and chemotherapy against colon tumors. The infiltration process was carried out using a post-synthetic methodology from an ethanol–**Cur** solution and the authors determined a maximum infiltration capacity of 0.5 mg mg^{-1} (1.36 μmol : 1.65 μmol).[16] Finally, in 2022, Munasinghe *et al.*, encapsulated **Cur** into **HKUST-1** to develop potential drug carriers' systems. To achieve this, the authors employed a post-synthetic methodology obtaining encapsulation efficiencies of 58.5 and 39.6% in low concentrations (5.9 ppm) and high concentrations (2845 ppm) after three days of exposure. In addition, the authors studied the interaction of **Cur** with the secondary building unit (SBU) of **HKUST-1**, concluding that the strongest interaction (30.5 kJ mol^{-1}) occurs through coordination bonds between the open metal sites and the hydroxyl groups of **Cur**.[17] Herein, it is worth noting that although there are several reports of the encapsulation of **Cur** into **HKUST-1**, most of them studied the infiltration process through a post-synthetic methodology, whereas the one-pot methodology is less explored, even when it is commonly known that the one-pot methodologies usually produce a more efficient infiltration.[18]

In addition to diminished light harvesting, the photocatalytic activity of **HKUST-1** is limited due to a low water stability. Indeed, we recently demonstrated that under photocatalytic conditions water molecules could replace other guest molecules such as DMF, decreasing the photocatalytic activity of **HKUST-1**. Additionally, the hydration of the material produced the formation of the linear coordination polymer CuBTC·3H_2O, which present decremented photocatalytic properties.[4] Therefore, in this contribution we propose the infiltration of **Cur** as an strategy to solve such water-stability problem in **HKUST-1**, since **Cur** is hydrophobic;[19] thus, if **Cur** is encapsulated in the cavities of **HKUST-1**, it could aid hindering water infiltration into the crystal lattice, retaining mainly the structural properties of the material for a longer period.

Therefore, in this work, we developed the *in situ* **Cur@HKUST-1** composite to enhance two important properties (i) light harvesting, and (ii) stability, aimed to improve the photocatalytic activity of **HKUST-1**. For light harvesting purposes, **Cur** presents a highly conjugated π structure to promote light absorption under the visible spectra, also providing energy level appropriated HOMO–LUMO orbitals for energy transfer purposes to the CB of **HKUST-1**. At the same time, we hypothesized that the hydrophobic structure of **Cur** strategically placed into the cavities of **HKUST-1** could enhance the stability of the host material.

2. Experimental section

2.1. Synthesis of HKUST-1 and Cur@HKUST-1 composites

The synthesis of **HKUST-1** was achieved following a one-pot and green process reported previously by our research group in 2013,[20] where 50 mg (0.24 mmol) of BTC and 604 mg of (0.72 mmol) sodium bicarbonate were weighed into a balloon flask; then, 20 mL of a mixture of ethanol/water (4 : 1) solvents

were added to the flask balloon to partially dissolve the powders. The suspension was stirred for 10 min to ensure homogeneity, but the powders were not fully dissolved, this partially produced the sodium trimesate. In another balloon flask was prepared a solution containing 67 mg (0.36 mmol) of copper(II) nitrate hemi(pentahydrate) dissolved in 10 mL of distilled water. This solution was added drop by drop to the suspension of BTC–3$NaHCO_3$, producing a blue powder instantaneously. Afterward, the new suspension was stirred for 24 h and maintained with vigorous reflux. Finally, the produced blue powder was recovered by simple filtration and dried in an electric furnace for 24 h at 100 °C, this yielded the **HKUST-1** material. Experimental data are in the ESI at SI1.†

For the synthesis of **Cur@HKUST-1** composite, the same method than that for **HKUST-1** was employed, with the only difference that in the ballon flask containing the BTC linker and $NaHCO_3$ also were added 9 mg of **Cur** (0.024 mmol), which is equivalent to 10% molar ratio of the BTC linker, and this variation produced the **Cur@HKUST-1**. Experimental data are located at SI1.†

2.2. Instrumental

The X-ray diffraction experiments for the synthesized powders (XRD) were conducted in a Bruker D2-phaser diffractometer (40 kV and 40 mA with CuKα radiation, λ = 1.5406 Å) in a 2θ range from 5° to 60° with a step size of 0.005° and an integration time of 6 s per step. For the identification of functional groups, a Bruker Alpha-2 FTIR spectrophotometer was employed, in a range of 4000–600 cm^{-1} with a resolution of 2 cm^{-1} at room temperature. The thermogravimetric analysis (TGA) was carried out using a PerkinElmer thermogravimetric analyzer model TGA-4000, in a temperature range from 25 to 900 °C, using nitrogen as the carrier gas and atmosphere. For the determination of **Cur** encapsulated into **HKUST-1**, the residual solvent mixture from the synthetic methodology were analyzed using UV-vis spectroscopy employing an IMPLEN GMBH spectrophotometer model NP80 Mobile, in a wavelength interval from 200 to 700 nm. The determination of the bandgap value was carried out by the Tauc plots constructed from the diffuse reflectance data obtained from UV-vis spectroscopy in the solid state. The spectrophotometer used for this means was a UV-vis NIR Cary 5000 model equipped with an integrating sphere for diffuse reflectance measurements. The hydrogen production was registered using a Thermo-Scientific gas chromatograph equipped with a thermal conductivity detector and a fused silica capillary column (30 m × 0.53 mm) using nitrogen as the carrier gas. In the photocatalytic and photo-electrochemical experiments, the samples were illuminated using a led lamp with emission in the visible region of the electromagnetic spectra, in the 400–700 nm interval (Lamp details: Gu10 6w 3000k 120v Philips Dimmable 400 Lumen).

2.3. Electrochemical measurements

The electrochemical tests were carried out employing a potentiotast/galvanostat AUTOLAB model PGSTAT302N with FRA module, using a conventional three electrode cell and the same lamp employed in the hydrogen production. An Ag/AgCl 3 M KCl electrode (0.207 *vs.* NHE) and a graphite sheet were employed as reference electrode and counter-electrode, respectively. For the construction of the working electrode, the materials were deposited on a conductive FTO substrate by a simple drop-coating method. To achieve this, a suspension composed of 20 mg of the materials, 2 mL of ethanol, and 20 μL of Nafion® resin solution was prepared; then, the suspension was dropped on the FTO surface. The photocurrents were registered at 0.746 V *vs.* RHE, for 600 s in intervals of 120 s in light and 120 s in darkness. In the same way, the electrochemical impedance spectroscopy (EIS) experiments were carried out at 0.746 V *vs.* RHE. These potentials are −0.1 V lower than the open-circuit potential (OCP) value of the materials and were imposed to achieve a more visible photocurrent derived from the activation of **Cur@HKUST-1** and **HKUST-1** under light irradiation and under the influence of an external potential. Finally, potentiodynamic electrochemical impedance (PEI) tests were carried out in a potential window without faradaic currents (from 0 to 1.6 V *vs.* RHE) at a frequency of 500 Hz.

2.4. Computational experiments

The encapsulation of **Cur** mainly in the open metal sites of **HKUST-1**, was achieved using the MOLDRAW software[21] in order to create the structural computational model of **Cur@HKUST-1**. The proposed initial geometry was completely relaxed (for angles and bond distances) to obtain the minimum energy structure (optimized geometry). The optimization of the initial geometry was carried out employing the antiferromagnetic phase of **HKUST-1**, according to that reported previously.[4] The calculation employed for the determination of the **Cur@HKUST-1** model was constructed with periodic boundary conditions and was computed in the CRYSTAL17 software[22] employing the hybrid functional HSE06[23] and the pob-DZVP basis set.[24,25] Geometry optimizations were obtained using a 2 × 2 Monkhorst–Pack, TOLINTEG was fixed in 7 7 7 9 30, which is the truncation criteria for bielectronic integrals. These values correspond to the overlap threshold for Coulomb, the penetration threshold for Coulomb, and the overlap threshold for HF exchange integrals, and the fourth and fifth parameters correspond to the pseudo overlap on the Hartree–Fock exchange series. The default values for optimization converge criteria were used.[26] The **Cur** structure was optimized in the software GAUSSIAN09,[27] employing as theory level the hybrid functional HSE06, and the cc-pVDZ basis set, and the HOMO–LUMO energies were determined. The software Avogadro[28] was employed to visualize the optimized structure of **Cur** and its HOMO–LUMO orbitals.

2.5. Photocatalytic experiments

For the photocatalytic hydrogen evolution experiments (see Scheme SI1†), 100 mg of the studied material (**HKUST-1** or **Cur@HKUST-1**) was dispersed into 200 mL of distilled water, employing a 250 mL Pyrex reactor as a container. The suspension was bubbled with nitrogen to eliminate all the oxygen dis-

solved; afterward, it was illuminated with visible light (400–700 nm) for 180 min, registering the produced hydrogen each 30 min. Herein, to determine the net photocatalytic activity of the studied **Cur@HKUST-1** composite, and to avoid adding more variables that could affect the photocatalytic activity of the studied materials, the employment of sacrificial agents was considered.[29–31]

3. Results and discussion

Herein the photosensitizer **Cur** was *in situ* infiltrated into the **HKUST-1** material to yield the **Cur@HKUST-1** composite, to determine if this conjoint would provide better photoelectrocatalytic behavior for the water splitting reaction to generate molecular hydrogen, in comparison to uninfiltrated **HKUST-1** material. The next sections would provide enough evidence to assure the obtaining of the **Cur@HKUST-1** composite, as follows.

3.1. UV-vis spectroscopic evidence of Cur infiltration into HKUST-1 and determination of infiltration degree

The residual solvents of the **Cur@HKUST-1** synthesis were measured through UV-vis spectroscopy to corroborate the infiltration degree of **Cur** into **HKUST-1**. The pure **Cur** in UV-vis spectral region showed two bands at 265 and 427 nm, which are attributed to $\pi \rightarrow \pi^*$ and a combination of $\pi \rightarrow \pi^*/n \rightarrow \pi^*$ transitions, respectively (Fig. 1a, orange line).[32]

Nevertheless, the bands observed in the residual solvent of the **Cur@HKUST-1** synthesis correspond to **Cur** coordinated to copper in solution and the positions of the observed bands shifted to different wavelengths (Fig. 1a, green line). Indeed, in the literature has been reported that the coordination of **Cur** with copper cause two maximums of absorption, and a decrement in the absorbance,[32,33] as we observed in the residual solvent of synthesis (Fig. 1a, black line).

Such a result indicated that the coordination of **Cur** with copper occurred since the initial stages in the synthesis of the **Cur@HKUST-1** composite due to the chelate effect. Thus, all the available **Cur** in the system should be coordinated, no matter that in solution and in the solid state. The one coordinated in the solid state is towards open metal sites in **HKUST-1** as adduct or chelate.

Because of these preliminary results observed in the experiments, the quantitative analysis of the infiltration degree was carried out by elaborating a new calibration curve including both **Cur** and Cu^{II} species in the same media. The new constructed curve was obtained by taking the absorbances of newly prepared solutions of Cu^{II} ions interacting with **Cur** at concentrations of 0.875, 1.75, 4.73, 8.75, and 17.5 ppm at 265 nm, in an stoichiometric amount of 1 : 1 [Cu^{II}]:.[28] The linear regression of the plot concentration *vs.* absorbance showed an R^2 of 0.999 (Fig. 1b), indicating a linear increment of the absorbance with the concentration of **Cur** → Cu^{II}. Thus, the model employed in the quantitative analysis of the infiltration of **Cur** to **HKUST-1** presented a high reliability.

The initial concentration of **Cur** in the reaction mixture was 875 ppm and after the synthesis process it was detected a final **Cur** concentration of 657 ppm, indicating the infiltration of 218 ppm, which corresponds to the 25% of the total **Cur** added to the reaction mixture. Such a result indicated a low infiltration degree since the initial amount of employed **Cur** was 10% molar (875 ppm) in relation to the linker BTC. Consequently, the infiltrated **Cur** corresponds only to the 2.5% molar (218 ppm) in relation to the BTC linker.

The obtained yield for **Cur@HKUST-1** composite was 62.7%, which was slightly lower (7.3%) than the observed for pristine **HKUST-1** (70%). The observed yield diminishment for the composite compared to **HKUST-1**, directly correlates with the amount of **Cur** → Cu^{II} coordination compound observed in the mother liquors (Fig. 1a, green line). Therefore, the 10% molar amount of guest molecule is coordinated towards Cu,

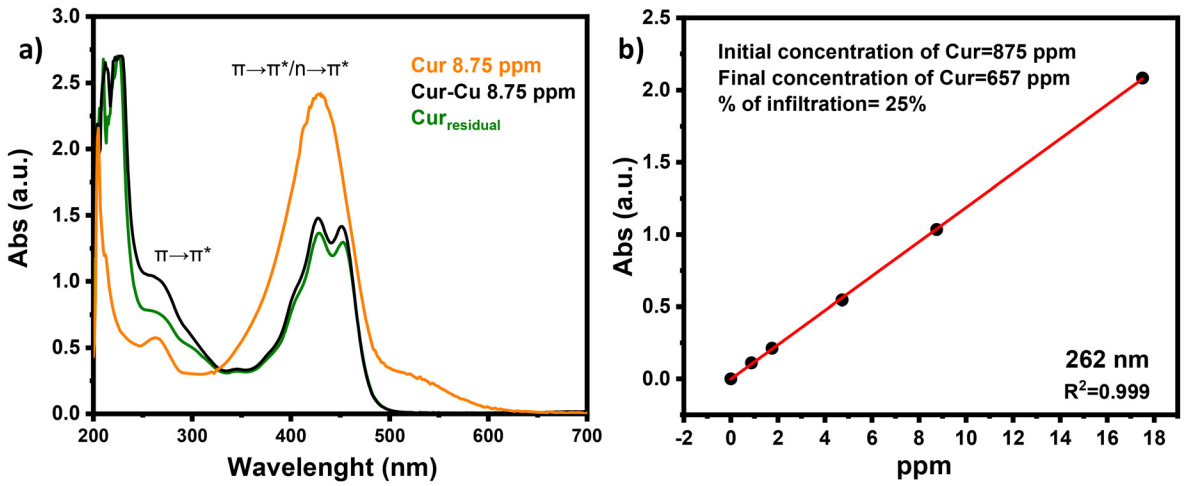

Fig. 1 (a) UV-vis spectra of pristine **Cur**, **Cur** → Cu^{II}, and **Cur** in the residual solvent of the **Cur@HKUST-1** synthesis. (b) Linear regression of the ppm *vs.* absorbance plot in an stoichiometric amount of the 1 : 1 [Cu^{II}]:[28] system measured at 262 nm by UV-vis spectroscopy.

ca. 7.5% in solution, and the remaining *ca.* 2.5% as the **Cur@HKUST-1** composite. The 7.5% contribution from the **Cur** → Cu^{II} coordination compound leads to a 7.5% reduction in available metallic centers for **HKUST-1** assembly, and consequently, a 7.5% lower composite yield. Evidence strongly indicates **Cur** → Cu^{II} in solution as the coordination compound and in the solid state as the **Cur@HKUST-1** composite.

3.2. X-ray diffraction analysis between HKUST-1 and Cur@HKUST-1

The diffractograms obtained from the crystalline powders of **Cur@HKUST-1** and bare **HKUST-1** and their comparison with the simulated XRD pattern of **HKUST-1** obtained from the CCDC (755080) are gathered in Fig. 2. Both **HKUST-1** and **Cur@HKUST-1** showed the typical diffraction peaks of this structure, confirming a successful synthesis. It is worth noting that **Cur@HKUST-1** has no additional diffraction peaks compared to **HKUST-1**, indicating that another crystalline phase of **Cur** is not present. Besides, we did not observe modifications in the structural parameters of **HKUST-1**, probably due to the low amount (*ca.* 2.5%) of infiltrated **Cur**. On the other hand, we calculated the crystallite size of **Cur@HKUST-1** and **HKUST-1** using the Scherrer equation, both presenting a crystallite size of 35 nm, indicating that the addition of **Cur** is not affecting the crystallinity of the composite. This parameter is important to analyze since it is well-known that a high crystallinity improves the charge transport in materials; thus, a decrement in crystallinity associated with the infiltration process could be undesirable for the photocatalytic properties of the final materials.[34]

3.3. FTIR spectroscopy, thermogravimetric, and microstructural analysis

We employed FTIR spectroscopy, thermogravimetric analysis (TGA), and microstructural characterization to confirm the successful synthesis of the **Cur@HKUST-1** composites and to elucidate the supramolecular host–guest interactions.

The FTIR spectra of the composite exhibited absorption bands corresponding to the characteristic functional groups of **HKUST-1**, confirming the formation of the host framework. No significant absorption bands attributable to **Cur** were detected, which was ascribed to the low degree of infiltration of the guest molecule, as determined by UV-Vis spectroscopy. Additionally, the FTIR analysis indicated a low content of both physisorbed and chemisorbed water, suggesting that **Cur** molecules replaced water in the MOF cavities, thereby confirming guest encapsulation.

Thermogravimetric analysis supported these findings by revealing a reduced amount of encapsulated water within the **HKUST-1** structure. A more detailed evaluation showed that chemisorbed water was displaced to a greater extent than physisorbed water upon **Cur** loading, implying that **Cur** preferentially occupies the open metal sites of the framework, which are typically associated with chemisorbed water. Moreover, the **Cur@HKUST-1** composite exhibited lower thermal stability compared to pristine **HKUST-1**, further corroborating the successful infiltration of **Cur** molecules.[35]

Finally, scanning electron microscopy (SEM) revealed notable changes in the microstructure of **HKUST-1** after the infiltration process. The modified morphology appeared more porous, which may influence key photocatalytic properties of the composite, such as its specific surface area.

Detailed analyses of these characterizations are provided in the ESI, sections SI2–SI4 (Fig. SI1–6, Table SI1).†

3.4. Textural properties

The N_2 adsorption–desorption isotherms (Fig. 3) were collected at −196.15 °C (77 K) for **HKUST-1** and **Cur@HKUST-1** (preactivated/degassed at 150 °C for 12 h) while the BET surface area of the materials and porosity properties are listed in Table 1. **HKUST-1** presented a type-1 isotherm, which is

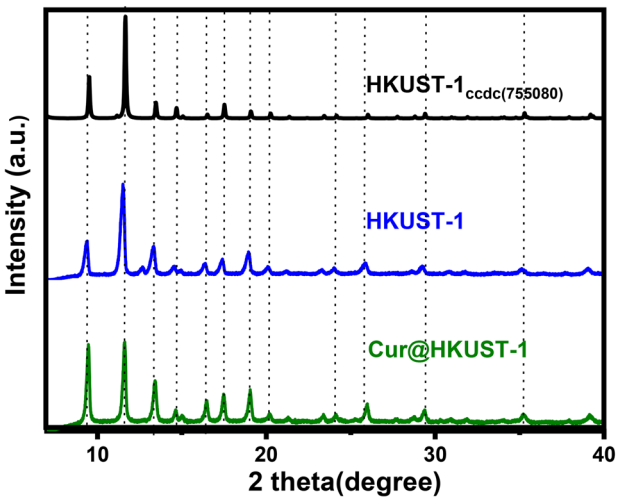

Fig. 2 Diffractograms of **Cur@HKUST-1** (green), **HKUST-1** (blue) synthesized in this work, and the **HKUST-1** monocrystal 755080 CCDC reference (black).

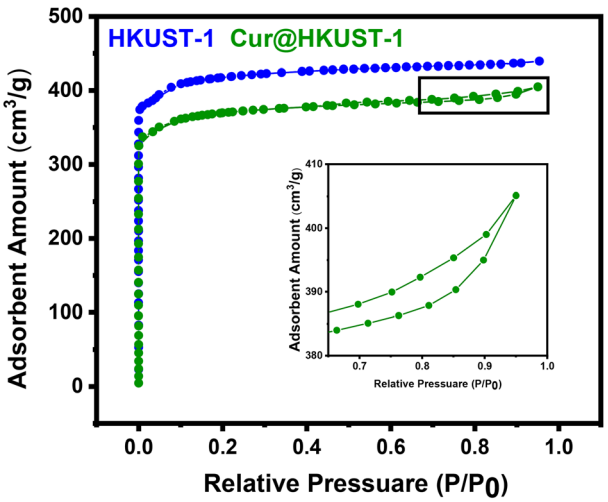

Fig. 3 Collected isotherms for **HKUST-1** and **Cur@HKUST-1**.

Table 1 Textural properties of **HKUST-1** and **Cur@HKUST-1**

MOF	S_{BET} ($m^2\ g^{-1}$)	V_m ($cm^3\ g^{-1}$)	Total pore volume ($cm^3\ g^{-1}$)	Average pore diameter (nm)
HKUST-1	970	223	0.68	2.8025
Cur@HKUST-1	863	198	0.63	2.9033

characteristic of (sub)microporous materials (pore diameters <2 nm),[36,37] as has been reported previously for this material.[38–40] In contrast, **Cur@HKUST-1** showed an initial part characteristic of type-I isotherms and a subsequent type-IV isotherm shape presenting a desorption branch with a pronounced N_2 hysteresis loop. The hysteresis loops observed in isotherms are related to pore (cavity) blocking, which is another piece of evidence suggesting the encapsulation of **Cur** into **HKUST-1**, cavitation could also explain the presence of hysteresis loops.[36–38] On the other hand, type-IV isotherms are characteristic of *meso*(macro)porous materials (pore diameter 2–50 nm and bigger).[36,37] This suggests that **Cur** induces additional porosity in the **Cur@HKUST-1** composite. The large, multifunctional **Cur** molecule likely contributes to this porosity both by partially inhibiting the growth of the original **HKUST-1** 3D architecture as a capping agent, and therefore by acting as a pore wall. The extent of this inhibition is related to the degree of **Cur** infiltration.

The calculated surface area of **HKUST-1** was 970 $m^2\ g^{-1}$, whereas **Cur@HKUT-1** presented a diminished surface area of 863 $m^2\ g^{-1}$. At the same time, the total pore volume of **HKUST-1** decreased from 0.68 in the pristine material to 0.63 $cm^3\ g^{-1}$ in the composite (≈7.35% diminishment), in agreement with TGA, corroborating the encapsulation of **Cur**. It is worth mentioning that a high surface area is beneficial for photocatalytic reactions since it increases the contact of the active sites with the reaction media. However, materials with high porosity, such as MOFs, could present a diminishment of photocatalytic activity due to a high porosity associated with a high volume of unpolarized void space, hindering the charge transport and promoting the recombination rate.[41] In this way, the decrement in the surface area of **Cur@HKUST-1** could be beneficial for photocatalytic properties and is also another piece of evidence confirming the encapsulation of the guest molecule. Regarding the average pore diameter, **HKUST-1** and **Cur@HKUST-1** presented similar values, 2.8 and 2.9 nm, evidencing that microporosity predominates over mesoporosity in **Cur@HKUST-1**.

3.5. Bandgap modulation determined by solid-state UV-vis spectroscopy

The Fig. 4a depicts the UV-vis spectra in solid state of **Cur@HKUST-1** and **HKUST-1**, denoting typical bands of **HKUST-1** at ≈300 and ≈700 nm, attributed to BTC → Cu and $Cu_{d(z^2)} \rightarrow Cu_{d(x^2-y^2)}$, electronic transitions.[42]

Nevertheless, **Cur@HKUST-1** presented a lower absorbance/quenching in the band attributed to $Cu_{d(z^2)} \rightarrow Cu_{d(x^2-y^2)}$ transition, suggesting a different chemical environment in the open metal sites. Thus, **Cur** interacting with open metal sites could be responsible for this effect, evidencing a possible **Cur** → Cu bonding scheme, and energy transfer from **Cur** to the CB of **HKUST-1**, composed mainly by the SBU.[4] The electronic transition $Cu_{d(z^2)} \rightarrow Cu_{d(x^2-y^2)}$ occurs due to the electronic transfer from the occupied $d(z^2)$ orbitals to the partially occupied $d(x^2 - y^2)$.[43] However, the coordination of guest species in the open metal sites must produce the interaction of rich-electron species with the partially occupied $d(x^2 - y^2)$ orbital, increasing its electronic density. Consequently, in the **Cur@HKUST-1** system the $d(x^2 - y^2)$ orbitals must have a

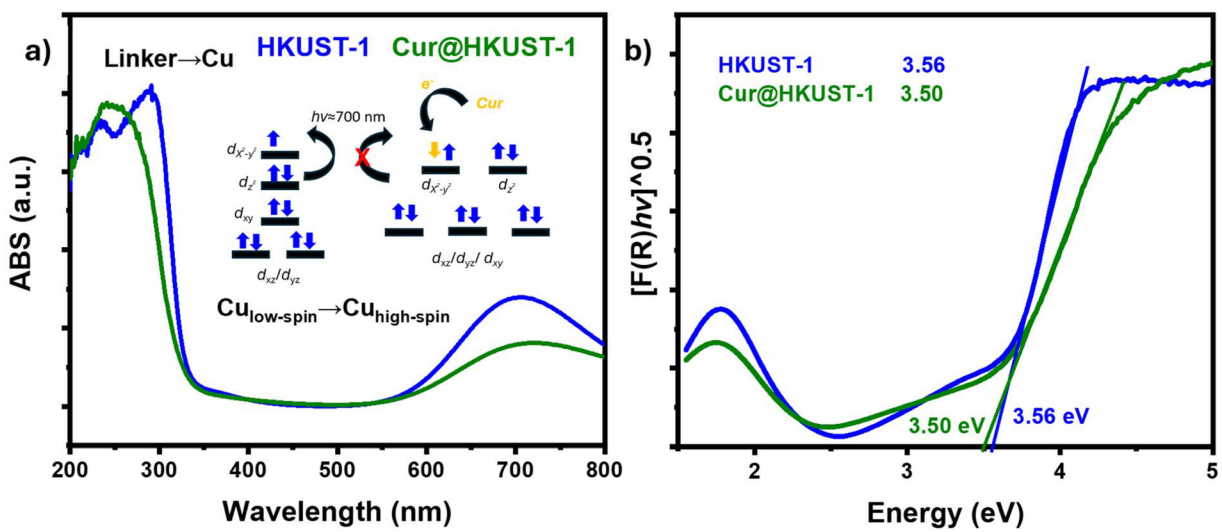

Fig. 4 For **HKUST-1** (blue line) and **Cur@HKUST-1** (green line): (a) UV-vis spectra, and energy orbitals diagram indicating comparative electronic promotion between the studied systems, as well as quenching of the band ≈700 nm, attributed to $Cu_{d(z^2)} \rightarrow Cu_{d(x^2-y^2)}$, due to the infiltration of **Cur**; (b) bandgap determination by Kubelka–Munk transformation, bandgap modulation due to infiltration of **Cur** was just slightly observed.

higher occupancy degree, avoiding the $Cu_{d(z^2)} \rightarrow Cu_{d(x^2-y^2)}$ transition and therefore decreasing the absorbance of this band, as we observed in the UV-vis spectra. Noteworthy, additional bands attributed to loaded **Cur** were absent probably due to the low infiltration degree.

Additionally, the optical bandgap of the materials was studied employing the Tauc plots (Fig. 4b) and eqn (1).

$$(F(R)h\nu)^n = A(h\nu - E_g) \quad (1)$$

where $F(R)$ is obtained from the Kubelka–Munk function, $h\nu$ is the energy of the incident photons, A is the absorbance, E_g is the bandgap value (eV), and n is a constant depending on the type of electronic transition, 1/2 for an allowed indirect electronic transition and 2 for an allowed electronic direct transition.[44] We calculated the bandgap value of **HKUST-1** and **Cur@HKUST-1** as an allowed indirect transition according to previous computational studies.[4] The encapsulation of **Cur** did not significantly modify the energy value of the transition BTC → Cu related to the inherent bandgap of **HKUST-1**. Indeed, an optical bandgap could not be determined due to the low infiltration degree obtained. Nevertheless, the sensitization effect occurs, but this evidence is going to be highlighted in the next sections.

3.6. Electrochemical experiments

Nonetheless that optical bandgap modulation due to **Cur** infiltration was not clearly observed (Fig. 4), the chronoamperometry experiments were employed to corroborate the sensitization effect of **Cur** toward **HKUST-1** (Fig. 5). To achieve this, **HKUST-1** and **Cur@HKUST-1** were supported on a conductive FTO glass employing simple dripping deposition; then, the (photo)currents of the materials were measured at −0.1 V related to the OCP of the studied materials (about 0.850 V *vs.* RHE). A reduction potential was imposed for comparative proposals since it is necessary to observe significative photocurrents to corroborate the sensitization effect. At the same time, a methodology of back-illumination was used since it diminishes the charge transport resistance of the film in the work-electrode, increasing the observed photocurrent.[45] Both materials presented an increment in the cathodic current, evidencing the excitation of electrons from the VB to the CB of **HKUST-1** and **Cur@HKUST-1** under visible light irradiation. Interestingly, **Cur@HKUST-1** presented a higher photocurrent than **HKUST-1**. This is suggesting an effect caused by the infiltrated **Cur** in the electrical and semiconductor properties of the **HKUST-1**, since the band gap value seems to be practically the same for both materials (Fig. 7). All this corroborates the photosensitizer effect of **Cur**, loaded into **HKUST-1**, and predicts a higher activity in photocatalytic applications. After a second irradiation cycle, both materials maintained practically the same photocurrent than the obtained in the first cycle, indicating a good photo-stability. Indeed, several published studies have employed this tool to corroborate the sensitization effect of related systems, although no new bands were observed in the UV-Vis spectra (Fig. 6).[11,46]

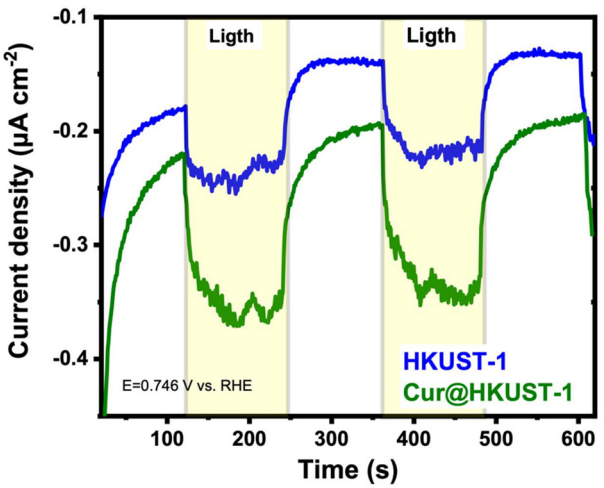

Fig. 5 Chronoamperometry experiments in light/darkness for **HKUST-1** and **Cur@HKUST-1**, evidencing an enhanced photosensitization for the composite.

Electrochemical Impedance Spectroscopy (EIS) was utilized to analyze the charge transfer resistance at the electrode–electrolyte interface. An increase in charge transfer resistance was observed suggesting a higher degree of charge recombination, which was attributed to the hydrophobic nature of the encapsulated **Cur**. This hydrophobic effect is thought to weaken the supramolecular interactions between **Cur@HKUST-1** and water (**Cur@HKUST-1**$\cdots$**H_2O**). These findings indicate that the encapsulation of guest species in MOFs, while beneficial in some aspects but may also negatively impact certain photocatalytic properties.

Despite the increased recombination, EIS also revealed an improvement in charge transport, a feature commonly associated with the infiltration of guest molecules into MOF structures. This dual behavior highlights the potential of **Cur**-loaded **HKUST-1** as a platform for the development of novel MOF-based conductive materials.

Potentiodynamic measurements confirmed that both pristine **HKUST-1** and the **Cur@HKUST-1** composite exhibit n-type semiconductor behavior, consistent with previous reports.[3,47,48] Furthermore, the encapsulation of **Cur** did not significantly alter the conduction band (CB) position of **HKUST-1**, and consequently, the valence band (VB) remained unchanged, see Fig. SI7.† The estimated redox potentials of the composite were 0.55 V (CB) and 4.0 V (VB) *versus* RHE, indicating that the material retains suitable redox potentials for driving the water-splitting reaction.[49]

Additionally, charge carrier density was estimated using the Mott–Schottky equation. The results showed a decrease in carrier concentration for the composite, in agreement with the EIS findings that suggested a higher charge recombination.

For a more detailed discussion of these characterizations, refer to SI5 (Fig. SI7 & Table SI2).†

3.7. Computational experiments

We proposed two geometric configurations for the **Cur@HKUST-1** composite, in which the encapsulated **Cur** can

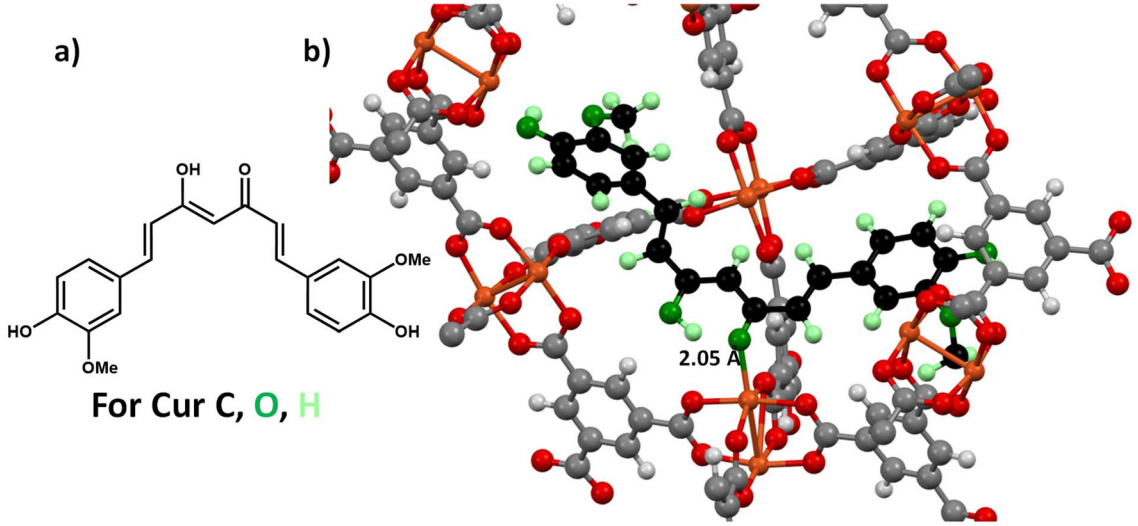

Fig. 6 (a) Chemical structure of the *cis–cis* rotamer of **Cur** and (b) optimized geometry for the **Cur**$_{cis-cis}$**@HKUST-1** composite.

adopt two distinct conformations. The first conformation, referred to as *cis–cis*, and the second, as *trans–trans*, were designated based on the structural arrangement of **Cur** (Fig. 6a and 7a, respectively).[50]

In Fig. 6 it is presented the optimized geometry for the **Cur**$_{cis-cis}$**@HKUST-1** composite. Although this geometry is less stable compared to the *trans–trans* geometry, it has been reported that this conformer could be stabilized in polar solvents such as water or ethanol, which are precisely the solvents employed in the synthesis of the studied **Cur@HKUST-1** composite.[51] The optimized geometry for the **Cur**$_{cis-cis}$**@HKUST-1** composite indicated that it is possible to store **Cur** in one single cavity of **HKUST-1** due to the compact structure of the *cis–cis* rotamer.[52] At the same time, the main supramolecular interaction detected in the **Cur**$_{cis-cis}$**@HKUST-1** system was a coordination bond type C═O$_{Cur}$ → Cu$_{HKUST-1}$ of about 2.05 Å, which is like the distance of the coordination bonds between the BTC linker and the Cu^{2+} cations (O_{BTC} → Cu, 1.93 Å), indicating similar stability. It is worth mentioning that in the **Cur**$_{cis-cis}$**@HKUST-1** system the coordinative bond C═O$_{Cur}$ → Cu$_{HKUST-1}$ is occupying one of the chemisorbed water sites, matching the TGA results.

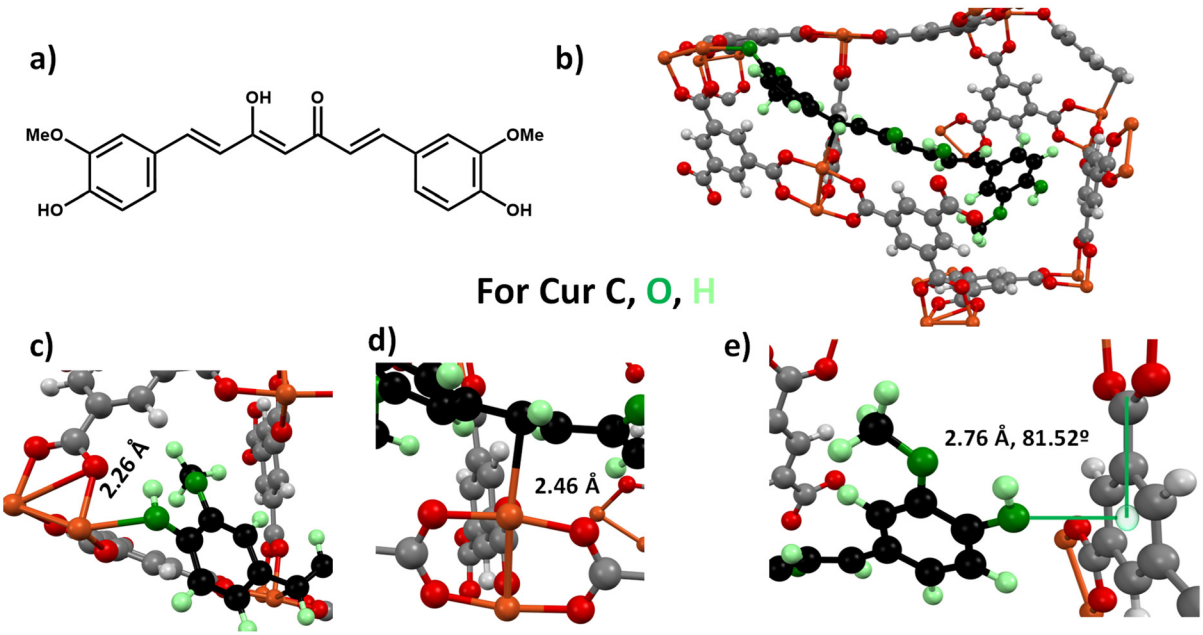

Fig. 7 (a) Chemical structure of the *trans–trans* rotamer of **Cur**. (b) Optimized structure of the system **Cur**$_{trans-trans}$**@HKUST-1**. Supramolecular interactions between **Cur** and **HKUST-1** (c) HO$_{Cur}$ → Cu$_{HKUST-1}$, (d) π_{Cur} → cation$_{CuHKUST-1}$, and (e) n_{HO-Cur} → $\pi_{HKUST-1}$.

In contrast, placing the *trans–trans* rotamer of **Cur** in **HKUST-1**, made it impossible to set this structure in just one **HKUST-1** cavity. Indeed, the optimized geometry for **Cur**$_{trans-trans}$**@HKUST-1** adopted a geometry placing it along two **HKUST-1** cavities, approximately occupying 1.5 cavities. This is possible since the cavities of **HKUST-1** are interconnected (Fig. 7b). On the other hand, Fig. 7c–e show the main supramolecular interactions associated with the infiltration of **Cur** into **HKUST-1**, which are a coordination bond $HO_{Cur} \rightarrow Cu_{HKUST-1}$ (distance 2.26 Å), a $\pi_{Cur} \rightarrow Cu_{HKUST-1}$ interaction (distance 2.46 Å), and a $n_{HO-CUR} \rightarrow \pi_{BTC-HKUST-1}$ interaction (distance 2.76 Å, angle 81.52°). It is worth emphasizing that the determined value for the latter interaction corresponds to those reported in the literature (distance 2.8–3.8 Å, $\angle \leq 90°$).[53] At the same time, the distances of these interactions are like the coordination bond distance of the $O_{BTC} \rightarrow Cu$ (1.93 Å), indicating a similar stability between these moieties.

This geometry required occupying two sites of chemisorbed water due to the coordination bonds between **Cur** and the open metal sites. The occupation of two open metal sites by **Cur** is higher than determined by TGA characterization, indicating that the **Cur**$_{cis-cis}$**@HKUST-1** shows a better agreement with the experimental results, consequently, this system makes the most significant contribution to the real structural configuration of the composite. However, the real value of chemisorbed water determined by TGA differs by a bit more than one water molecule in the original **HKUST-1** compared to the **Cur@HKUST-1** composite. Thus, the difference between the experimental and the theoretical values for the **Cur**$_{cis-cis}$**@HKUST-1** system is attributed to a small amount of **Cur**$_{trans-trans}$**@HKUST-1** system in the real structure of the composite.

Following our results, Munasinghe *et al.*, determined that the encapsulation of **Cur** into **HKUST-1** occurs through the formation of a coordination bond type $HO_{Cur} \rightarrow Cu_{HKUST-1}$ and $C{=}O_{Cur} \rightarrow Cu_{HKUST-1}$. Nevertheless, these previous geometries employed only partial structural models using the SBU of **HKUST-1** without periodic boundary conditions.[17]

Finally, a comparison between the structural parameters of **HKUST-1** (**HKUST-1**$_{NS}$), **Cur**$_{cis-cis}$**@HKUST-1**, and **Cur**$_{trans-trans}$**@HKUST-1** is presented in section SI6 (Fig. SI8 & Table SI3).†

The HOMO–LUMO of **Cur** were calculated to understand a possible mechanism of sensitization promoted by **Cur** that was observed and discussed in the electrochemical section. Both the HOMO and LUMO orbitals are localized along all the carbons and oxygens composing the structure of **Cur**, except for the $-CH_3$ groups in the methoxides (Fig. 8). The calculated energies for these orbitals were −5.26 and −2.41 eV, respectively, matching the previously reported values in the literature (−5.76 and −2.76 eV).[10] With these, the determined HOMO–LUMO gap for **Cur** is 2.85 eV, which corresponds to a wavelength of 435 nm, being in the visible region of the electromagnetic spectrum confirming the sensitizing effect promoted by **Cur**. Meanwhile, the energies of the VB and CB of **HKUST-1** were −7.19 and −3.16 eV, respectively.

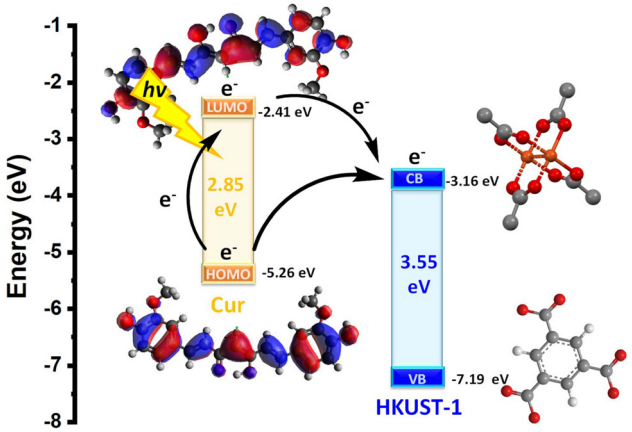

Fig. 8 Charge transfer mechanism proposed for the **Cur@HKUST-1** composite.

In this way, the plausible mechanism of charge transfer should imply the excitation of electrons between HOMO–LUMO in **Cur** and subsequent electron transfer from $LUMO_{Cur}$ to $CB_{HKUST-1}$, according to that described in the literature, related to the sensitization effect.[9] Therefore, in the photocatalytic process, oxidant species should be localized in the $HOMO_{Cur}$, whereas the reduction process should occur only in the SBU of **HKUST-1**. Indeed, the transference of electrons from $HOMO_{Cur}$ to $CB_{HKUST-1}$ could be facilitated due to the short distance between the atoms composing $HOMO_{Cur}$ and the SBU of **HKUST-1**, composing the CB,[4] by $C{=}O_{Cur} \rightarrow Cu_{HKUST-1}$ or $C\text{-}(H)O_{Cur} \rightarrow Cu_{HKUST-1}$ interactions.

3.8. Photocatalytic test

To track the effectiveness of **Cur** in enhancing light harvesting and photocatalytic activity of **HKUST-1**, the developed materials were evaluated toward photocatalytic hydrogen evolution (PHE). Such a reaction is crucial to reach a sustainable society due to hydrogen is a clean or green fuel just providing water as combustion product, with higher energetic power than fossil fuels.[54] These tests were conducted to evaluate a direct sensitization effect of **Cur** in **HKUST-1**, without the usage of sacrificial agents, mainly to avoid any potential masking due to other possible interactions (sacrificial agent···**Cur@HKUST-1**). The results indicated that **Cur@HKUST-1** developed a higher photocatalytic activity compared to **HKUST-1**, corroborating the effectiveness of **Cur** enhancing light harvesting. In the first 60 min of the reaction, **Cur@HKUST-1** presented a hydrogen evolution 1.2 times higher than **HKUST-1** (585 *vs.* 483 μmol g^{-1}, respectively) just by infiltrating 2.5% of **Cur** into the **HKUST-1**. Nevertheless, as the reaction advanced, the photocatalytic activity of both materials decreased, indicating instability (Fig. 9). For comparison purposes, we previously determined the photocatalytic activity of similar systems **H$_2$O@HKUST-1** and **DMF@HKUST-1**, which presented practically the same hydrogen evolution after 180 min of reaction.[4] Therefore, the **Cur@HKUST-1** composite clearly evidenced higher photo-

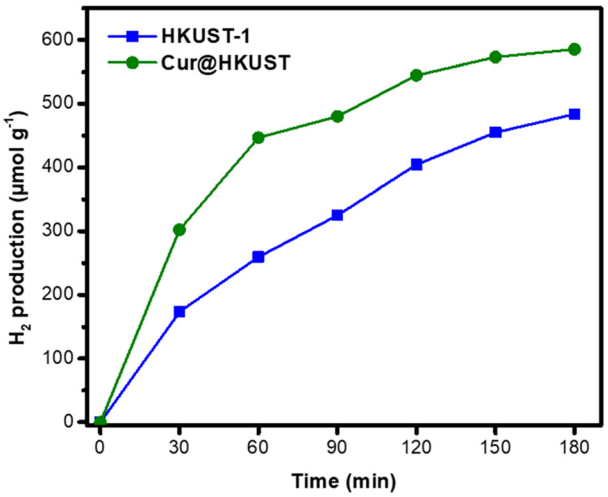

Fig. 9 Photocatalytic hydrogen evolution determined for **HKUST-1** and **Cur@HKUST-1**.

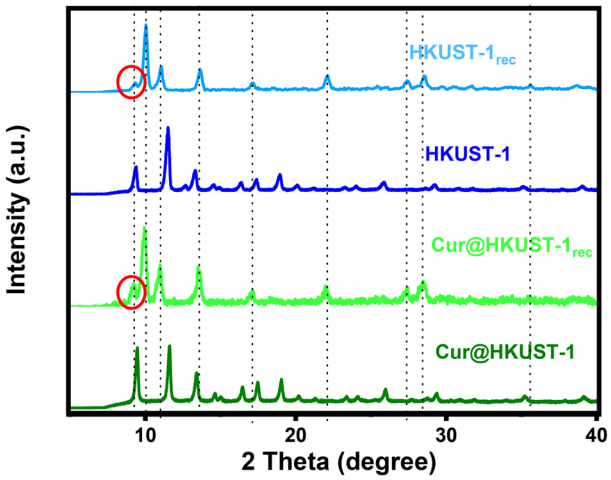

Fig. 10 XRD patterns of **Cur@HKUST-1**, **HKUST-1**, **Cur@HKUST-1$_{REC}$**, and **HKUST-1$_{REC}$**. The plane (2 2 0) attributed to **HKUST-1** was highlighted with a red circle.

catalytic activity than pristine **HKUST-1** (**H_2O@HKUST-1**), demonstrating a higher stability of the **Cur@HKUST-1** system in comparison to **DMF@HKUST-1**. Such a result is attributed to the hydrophobic environment promoted by **Cur** in the whole material, surface and cavities, and corroborated through TGA, FTIR, and EIS.

3.9. Stability evaluation of the composite

As it was mentioned in the Introduction section, the conditions for photocatalytic reactions led to the formation of the linear coordination polymer CuBTC·3H_2O, developing decreased photocatalytic properties compared to **HKUST-1**.[4] This phase transition occurred due to the infiltration of water in the crystal lattice of the host, diminishing its dimensionality from 3D to 1D, therefore releasing the guest molecules in the cavities, such as residual solvents, for example, DMF.[4] To demonstrate the higher stability of **Cur@HKUST-1** compared to bare **HKUST-1**, XRD experiments were carried on with the recovered powders (**Cur@HKUST-1$_{REC}$** and **HKUST-1$_{REC}$**, respectively) from the photocatalytic reaction described in the previous section (Fig. 10). In addition, **Cur@HKUST-1$_{REC}$** and **HKUST-1$_{REC}$** were also compared with **DMF@HKUST-1$_{REC}$** described in our earlier work.[4] In the diffractograms of the mentioned materials, the appearance of the CuBTC·3H_2O crystalline phase suggested structural instability in all three materials. Nevertheless, the plane (2 2 0) detected at 9° (2θ) was attributed to residual **HKUST-1** in all the diffractograms. Therefore, to quantify the residual proportion of **HKUST-1** for the active materials, it was carried out the determination of the area below the curve of these peaks and the peaks related to CuBTC·3H_2O. By this means, we determined the residual proportions of **Cur@HKUST-1$_{REC}$**, **HKUST-1$_{REC}$**, and **DMF@HKUST-1$_{REC}$** being of 9.9, 5.9, and 4.7%, respectively. Consequently, the infiltration of 2.5% of **Cur** into **HKUST-1** maintained in a higher extent the initial structure of **HKUST-1** before the activity test of the initial materials in 69.9 and 114% compared with **HKUST-1$_{REC}$** and **DMF@HKUST-1$_{REC}$**, respectively. We attributed such a result to the hydrophobic environment provided by **Cur**, which hinders the infiltration of water into **HKUST-1**, as it was stipulated in our initial hypothesis. It is worth emphasizing that even though **Cur@HKUST-1** is still an unstable material, the observed results confirmed that the infiltration of guest species into MOFs pores and cavities resulted a suitable strategy to enhance its stability. Therefore, this result represents a further step in the correct direction to develop photocatalytic systems based on MOFs with enhanced stability.

Four reaction cycles were evaluated (Fig. 11) to investigate the stability of the **Cur@HKUST-1** composite. After each cycle, a progressive decrease in photocatalytic activity was observed, consistent with experimental characterization indicating the instability of the material under hydrogen evolution conditions. Nevertheless, although the chemical structure of **Cur@HKUST-1** is modified during the photochemical reaction, the resulting composite material—CuBTC·3H_2O (90%)/**Cur@HKUST-1** (10%)—exhibited photocatalytic activity comparable to that of pristine **HKUST-1**, particularly during the second reaction cycle. These findings suggest that the infiltration of curcumin into **HKUST-1** contributes to attain an improved stability.

3.10. Comparison of Cur@HKUST-1 with other MOF systems for photocatalytic hydrogen evolution

Making a direct comparison between the photocatalytic activities of different MOFs and related materials is challenging mainly because their variable stabilities in water.[55] Therefore, MOF's stability and the experimental conditions, including the use of sacrificial agents, significantly affect hydrogen production. Hence, to assess a fair contrast about the hydrogen evolution rate (HER [=] μmol h^{-1} g^{-1}) of the current **Cur@HKUST-1** composite against similar materials is worth to

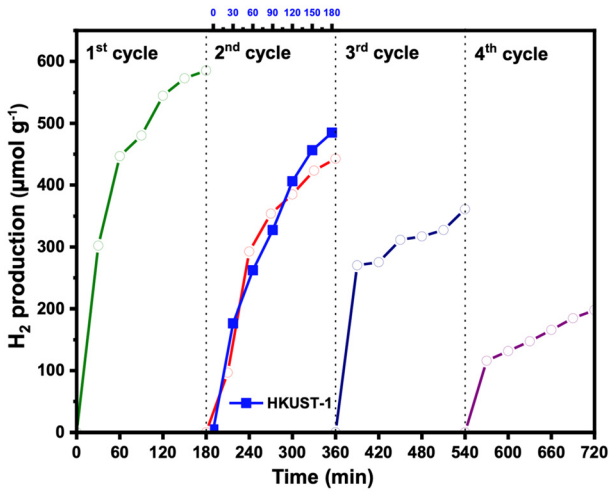

Fig. 11 Photocatalytic hydrogen evolution of **Cur@HKUST-1** after four reaction cycles (1st cycle green, 2nd cycle red, 3rd cycle dark blue, 4th cycle purple; **HKUST-1** was just assessed the 1st cycle, light blue).

stipulate that the composite of study has been irradiated with visible light, in comparison with other materials that have been irradiated with UV, or UV-vis light sources, this mainly due to the photosensitizing nature of **Cur**. Some of the best systems for this means of developing high HER are heterostructures (Pt_{NP}@Pd–PCN-222(Hf) HER = 22 674, MOF-808@TpPa-1-COF (6/4) HER = 11 880) or heterojunctions (Pt@MIL-125/Au HER = 265), often including very expensive additions such as Pt, Pd, Hf, Au, their combinations (Pt_{NP}@Pd–PCN-222(Hf)), among others, this in comparison with **Cur**, which is an organic compound and of a cheaper nature. Table 2 gathers some comparisons of bare materials with very good HER values, and some other materials with varying HER values, that were enhanced by the inclusion of sensitizing agents, as is the case of **Cur@HKUST-1** composite. Just to emphasize the usefulness of the infiltration strategy, also in this table are very good examples of HER increment due to this infiltrant@MOF strategy, *e.g.* the PCN-222(Hf) system that has not observable HER, to the final engineered structure of the Pt_{NP}@Pd–PCN-222(Hf), where the inclusion of Pd metals in the cavity of the porphyrinic ligand turned on the HER to reach 2476, and finally with the inclusion of platinum nanoparticles (Pt_{NP}) to the highest HER value of 22 674. Some other more modest examples are the PCN-9(Co) that with the inclusion of Pt^{4+} enhanced the HER from 4.8 to 33.5, or the case of BDC–Zn with HER of 47.5, to the relatives with methyl orange or methylene blue that reached 1138 and 1259, respectively. To finally reach the current example, where **HKUST-1** provided a HER of 161, and the infiltrated system **Cur@HKUST-1**, augmented to 195, just by a 2.5% infiltration of the **Cur** sensitizer, also providing augmented stability in the composite. All these comparisons and analysis clearly revealed that the infiltration of species in reticular systems, as the MOFs, is a very powerful strategy to obtain emergent properties such as the photocatalytic hydrogen evolution.

Table 2 Hydrogen evolution rate (HER) comparison for **Cur@HKUST-1** and related materials

Material	H_2 evolution rate (HER) [μmol h^{-1} g^{-1}]	Ref.
MIL-125–NH_2	4327	56
Pt@MIL-125/Au Schottky junctions	265	57
PCN-9(Co)	4.8	58
Pt^{4+}@PCN-9(Co)	33.5	
BDC–Zn	47.5	59
(Methyl orange)@BDC–Zn	1137.8	
(Methylene blue)@BDC–Zn	1259.4	
MoS_2@ZIF-8	68.4	60
TpPa-1-COF	2121	61
MOF-808@TpPa-1-COF (6/4, MOF–COF hybrid heterostructure)	11 880	
Pt_{NP}@MIL-100(Fe)	98	62
Pt_{NP}@UiO66–NH_2(Zr)	257	
Pt_{NP}@MIL-125–NH_2(Ti)	367	
Pt_{NP}@Pd–PCN-222(Hf)	22 674	
Pd–PCN-222(Hf)	2476	
PCN-222(Hf)	Not observable	
HKUST-1	161[a]	This work
Cur@HKUST-1	195[a]	

[a] 1st cycle of HER lasting 3 h, see Fig. 11.

4. Conclusions

The infiltration of 2.5% of **Cur** into **HKUST-1** was achieved successfully. The main evidence that confirms the encapsulation of **Cur** into **HKUST-1** is a decrement in the thermal stability and surface area of **Cur@HKUST-1** compared to bare **HKUST-1**. At the same time, the preservation of the **HKUST-1** structure in the **Cur@HKUST-1** composite was demonstrated by XRD and FTIR experiments.

The infiltration degree of 2.5% in the **Cur@HKUST-1** composite was determined by UV-Vis experiments, indicating a low affinity of **HKUST-1** toward **Cur**, since an initial amount of 10% mol was employed, still just one quarter of this was loaded. This could be due to the inherent steric hindrance of the large guest, whether that *cis–cis* or *trans–trans* **Cur** rotamers were assessed.

Employed characterization tools indicated that encapsulated **Cur** is coordinated to the open metal sites of **HKUST-1**; provoking different effects in the **Cur@HKUST-1** composite:

(i) **Cur** in residual solvents is coordinated to copper, indicating a high affinity of the guest molecule toward the open metal sites.

(ii) TGA indicated a lower amount of chemisorbed water, compared with bare **HKUST-1**.

(iii) UV-vis experiments in the solid state showed a quenching effect of the band attributed to the transitions $Cu_{d(z^2)} \rightarrow Cu_{d(x^2-y^2)}$, which depends on the chemical environment in the SBU (open metal sites), an effect attributed to **Cur** → $Cu_{HKUST-1}$ interaction.

(iv) The optimized geometries calculated for **Cur@HKUST-1** using DFT methods in periodic boundary conditions indicated that the coordination of OH/C=O groups in **Cur** to open metal

sites in **HKUST-1**, resulted the lowest energy geometries for the **Cur$_{trans-trans}$@HKUST-1** or **Cur$_{cis-cis}$@HKUST-1**, respectively.

In chronoamperometry experiments under visible light irradiation, **Cur@HKUST-1** presented a higher current density than pristine **HKUST-1**, corroborating the sensitization effect. Consequently, **Cur@HKUST-1** also produces a higher hydrogen evolution rate (HER) than pristine **HKUST-1**, demonstrating the effectiveness of infiltration as a strategy to develop materials with enhanced visible light harvesting.

Nevertheless, **Cur's** infiltration incremented the charge transference resistance observed through EIS experiments and MS plots; thus, infiltration could also decrease or modify some photocatalytic properties of materials.

Finally, the **Cur@HKUST-1** composite exhibited an increase in conductivity, compared with **HKUST-1**, signifying an important emerging property that could be further exploited without the employment of expensive infiltrators, and ecofriendly as is the case of **Cur**.

Data availability

The data that support the findings of this study are available in the ESI† of this article. Any other information should be requested to the corresponding authors.

Conflicts of interest

The authors certify that they have NO affiliations with or involvement in any organization or entity with any financial or non-financial interest in the subject matter or materials discussed in this manuscript.

Acknowledgements

This work was supported by UANL to direct funding, and UAM for the funding through the Research Project UAM-A, DCBI number CB005-22. We also acknowledge to "Laboratorio de Supercómputo y Visualización en Paralelo" UAM Iztapalapa, for the computational facilities provided to develop the theoretical section of this contribution. LAAH and JSRG thank CONACyT for the Ph.D. degree scholarships numbers 821611 and 824115, respectively. JSRG (CVU 824115) acknowledges the postdoctoral fellowship EPM 2024 (1) provided by CONAHCyT/SECIHTI.

References

1 J. Zhang, *et al.*, Enhanced visible light photocatalytic degradation of dyes in aqueous solution activated by HKUST-1: performance and mechanism, *RSC Adv.*, 2020, **10**(61), 37028–37034.
2 T. Ma, *et al.*, II-Scheme Heterojunction Frameworks Based on Covalent Organic Frameworks and HKUST-1 for Boosting Photocatalytic Hydrogen Evolution, *ChemSusChem*, 2024, **17**(22), e202400987.
3 L. A. Alfonso Herrera, *et al.*, Elucidating, understanding, and correlating the (photo)electrochemical and physicochemical properties of HKUST-1 through an experimental and computational approach, *New J. Chem.*, 2024, 11377–11386.
4 L. A. Alfonso-Herrera, *et al.*, Elucidating structural stability, bandgap, and photocatalytic hydrogen evolution of (H_2O/DMF)@HKUST-1 host-guest systems, *ChemPlusChem*, 2024, e202300579.
5 A. Raeisi, A. Najafi Chermahini and M. M. Momeni, A novel photocatalytic and photoelectrocatalytic system for oxidative desulfurization of model fuel using BiVO4@HKUST-1 composite in powder and deposited on fluorine-doped tin oxide, *J. Photochem. Photobiol., A*, 2022, **433**, 114190.
6 L. Huang, *et al.*, A light-driven enzyme-free photoelectrochemical sensor based on HKUST-1 derived Cu2O/Cu@microporous carbon with g-C3N4 p-n heterojunction for ultra-sensitive detection of l-cysteine, *Carbon*, 2023, **215**, 118466.
7 Y. Wu, *et al.*, Core-shell structured Cu2O@HKUST-1 heterojunction photocatalyst with robust stability for highly efficient tetracycline hydrochloride degradation under visible light, *Chem. Eng. J.*, 2021, **426**, 131255.
8 X. Li, *et al.*, Mesopores octahedron GCNOX/Cu2O@C inhibited photo-corrosion as an efficient visible-light catalyst derived from oxidized g-C3N4/HKUST-1 composite structure, *Appl. Surf. Sci.*, 2020, **510**, 145459.
9 J. Diaz-Angulo, *et al.*, Visible-light activation of TiO2 by dye-sensitization for degradation of pharmaceutical compounds, *Photochem. Photobiol. Sci.*, 2019, **18**(4), 897–904.
10 E. Gál and L. C. Nagy, Photophysical Properties and Electronic Structure of Symmetrical Curcumin Analogues and Their BF2 Complexes, Including a Phenothiazine Substituted Derivative, *Symmetry*, 2021, **13**(12), 2299.
11 J. Lim, A. D. Bokare and W. Choi, Visible light sensitization of TiO2 nanoparticles by a dietary pigment, curcumin, for environmental photochemical transformations, *RSC Adv.*, 2017, **7**(52), 32488–32495.
12 H. S. Kushwaha and R. Vaish, Enhanced Visible Light Photocatalytic Activity of Curcumin-Sensitized Perovskite Bi0.5Na0.5TiO3 for Rhodamine 6G Degradation, *Int. J. Appl. Ceram. Technol.*, 2016, **13**(2), 333–339.
13 Z. Yan, *et al.*, Curcumin Doped SiO_2/TiO2 Nanocomposites for Enhanced Photocatalytic Reduction of Cr(VI) under Visible Light, *Catalysts*, 2020, **10**(8), 942.
14 F. M. Khandan, *et al.*, Novel uranyl-curcumin-MOF photocatalysts with highly performance photocatalytic activity toward the degradation of phenol red from aqueous solution: effective synthesis route, design and a controllable systematic study, *J. Mater. Sci.: Mater. Electron.*, 2018, **29**(21), 18600–18613.

15 L. Yang, *et al.*, Remodeling microenvironment based on MOFs-Hydrogel hybrid system for improving diabetic wound healing, *Chem. Eng. J.*, 2022, **427**, 131506.
16 Q. Tian, *et al.*, Engineering of an endogenous hydrogen sulfide responsive smart agent for photoacoustic imaging-guided combination of photothermal therapy and chemotherapy for colon cancer, *J. Adv. Res.*, 2022, **41**, 159–168.
17 V. K. Munasinghe, *et al.*, Impact of active sites on encapsulation of curcumin in Metal Organic Frameworks, *Mater. Res. Express*, 2023, **10**(3), 035102.
18 L.Á. Alfonso Herrera and H. I. Beltrán, Infiltration as a frontier bandgap engineering strategy in MOFs: A critical review, *Coord. Chem. Rev.*, 2024, **505**, 215658.
19 Á. Arango-Ruiz, *et al.*, Encapsulation of curcumin using supercritical antisolvent (SAS) technology to improve its stability and solubility in water, *Food Chem.*, 2018, **258**, 156–163.
20 S. Loera-Serna, *et al.*, An alkaline one-pot metathesis reaction to give a [Cu3(BTC)2] MOF at r.t., with free Cu coordination sites and enhanced hydrogen uptake properties, *RSC Adv.*, 2013, **3**(27), 10962–10972.
21 P. Ugliengo, D. Viterbo and G. Chiari, MOLDRAW: Molecular graphics on a personal computer, *Z. fur Krist. – Cryst. Mater.*, 1993, **207**(1), 9–24.
22 R. Dovesi, *et al.*, Quantum-mechanical condensed matter simulations with CRYSTAL, *Wiley Interdiscip. Rev.:Comput. Mol. Sci.*, 2018, **8**(4), e1360.
23 M. F. Peintinger, D. V. Oliveira and T. Bredow, Consistent Gaussian basis sets of triple-zeta valence with polarization quality for solid-state calculations, *J. Comput. Chem.*, 2013, **34**(6), 451–459.
24 A. V. Krukau, *et al.*, Influence of the exchange screening parameter on the performance of screened hybrid functionals, *J. Chem. Phys.*, 2006, **125**(22), 224106.
25 J. P. Perdew, K. Burke and M. Ernzerhof, Generalized Gradient Approximation Made Simple, *Phys. Rev. Lett.*, 1996, **77**(18), 3865–3868.
26 R. Dovesi, *et al.*, CRYSTAL: a computational tool for the ab initio study of the electronic properties of crystals, *Z. Kristallogr. - Cryst. Mater.*, 2005, **220**(5–6), 571–573.
27 M. J. Frisch, et al., *Gaussian 16 Rev. C.01*, 2016, Wallingford, CT.
28 M. D. Hanwell, *et al.*, Avogadro: an advanced semantic chemical editor, visualization, and analysis platform, *J. Cheminf.*, 2012, **4**(1), 17.
29 S. Qiao, *et al.*, Conjugated porous polymers for photocatalysis: The road from catalytic mechanism, molecular structure to advanced applications, *EnergyChem*, 2022, **4**(6), 100094.
30 T. Zhang and S. Lu, Sacrificial agents for photocatalytic hydrogen production: Effects, cost, and development, *Chem Catal.*, 2022, **2**(7), 1502–1505.
31 V. Kumaravel, *et al.*, Photocatalytic Hydrogen Production: Role of Sacrificial Reagents on the Activity of Oxide, Carbon, and Sulfide Catalysts, *Catalysts*, 2019, **9**(3), 276.
32 E. H. Ismail, *et al.*, Synthesis and Characterization of some Ternary Metal Complexes of Curcumin with 1,10-phenanthroline and their Anticancer Applications, *J. Sci. Res.*, 2014, **6**(3), 509–519.
33 S. Vellampatti, *et al.*, Metallo-Curcumin-Conjugated DNA Complexes Induces Preferential Prostate Cancer Cells Cytotoxicity and Pause Growth of Bacterial Cells, *Sci. Rep.*, 2018, **8**(1), 14929.
34 L. G. Devi, B. N. Murthy and S. G. Kumar, Photocatalytic activity of TiO2 doped with Zn2+ and V5+ transition metal ions: Influence of crystallite size and dopant electronic configuration on photocatalytic activity, *Mater. Sci. Eng., B*, 2010, **166**(1), 1–6.
35 S. Loera-Serna, E. Ortiz and H. I. Beltrán, First trial and physicochemical studies on the loading of Basic Fuchsin, Crystal Violet and Black Eriochrome T on HKUST-1, *New J. Chem.*, 2017, **41**(8), 3097–3105.
36 M. Thommes, *et al.*, Physisorption of gases, with special reference to the evaluation of surface area and pore size distribution (IUPAC Technical Report), *Pure Appl. Chem.*, 2015, **87**(9–10), 1051–1069.
37 S. Çakar and M. Özacar, The effect of iron complexes of quercetin on dye-sensitized solar cell efficiency, *J. Photochem. Photobiol., A*, 2017, **346**, 512–522.
38 S. Loera-Serna, *et al.*, Composites of Anthraquinone Dyes@HKUST-1 with Tunable Microstructuring: Experimental and Theoretical Interaction Studies, *Chem. – Eur. J.*, 2019, **25**(17), 4398–4411.
39 Y. Chen, *et al.*, High efficiency synthesis of HKUST-1 under mild conditions with high BET surface area and CO2 uptake capacity, *Prog. Nat. Sci.:Mater. Int.*, 2018, **28**(5), 584–589.
40 T. Toyao, *et al.*, Positioning of the HKUST-1 metal–organic framework (Cu3(BTC)2) through conversion from insoluble Cu-based precursors, *Inorg. Chem. Front.*, 2015, **2**(5), 434–441.
41 R. Scatena, Y. T. Guntern and P. Macchi, Electron Density and Dielectric Properties of Highly Porous MOFs: Binding and Mobility of Guest Molecules in Cu3(BTC)2 and Zn3(BTC)2, *J. Am. Chem. Soc.*, 2019, **141**(23), 9382–9390.
42 M. Karimi, *et al.*, Fluorinated solvent-assisted photocatalytic aerobic oxidative amidation of alcohols via visible-light-mediated HKUST-1/Cs-POMoW catalysis, *New J. Chem.*, 2021, **45**(31), 14024–14035.
43 C. H. Hendon and A. Walsh, Chemical principles underpinning the performance of the metal–organic framework HKUST-1, *Chem. Sci.*, 2015, **6**(7), 3674–3683.
44 V. Sabaghi, *et al.*, Synthesis and evaluation of pH-responsive mesoporous ZnO/PEG/DOX nanocomposite based on Zn-HKUST-1 MOF nanostructure for targeted drug delivery, *J. Porous Mater.*, 2022, **30**(1), 201–209.
45 J. E. Carrera-Crespo, *et al.*, Unrevealing the effect of transparent fluorine-doped tin oxide (FTO) substrate and irradiance configuration to unmask the activity of FTO-BiVO4 heterojunction, *Mater. Sci. Semicond. Process.*, 2021, **128**, 105717.
46 K. Mohammadi, *et al.*, Photoelectrochemical activity of Ag loaded TiO2 nanotube arrays produced by sequential

chemical bath deposition for water splitting, *J. Mater. Sci.: Mater. Electron.*, 2019, **30**(2), 1878–1884.

47 S. Mosleh, *et al.*, Ce/Eu redox couple functionalized HKUST-1 MOF insight to sono-photodegradation of malathion, *J. Hazard. Mater.*, 2021, **409**, 124478.

48 X. Li, *et al.*, Mesopores octahedron GCNOX/Cu2O@C inhibited photo-corrosion as an efficient visible-light catalyst derived from oxidized g-C3N4/HKUST-1 composite structure, *Appl. Surf. Sci.*, 2020, **510**, 145459.

49 R. Sharifian, *et al.*, Electrochemical carbon dioxide capture to close the carbon cycle, *Energy Environ. Sci.*, 2021, **14**(2), 781–814.

50 P. Chatterjee, S. S. Dutta and T. Chakraborty, Tautomers and Rotamers of Curcumin: A Combined UV Spectroscopy, High-Performance Liquid Chromatography, Ion Mobility Mass Spectrometry, and Electronic Structure Theory Study, *J. Phys. Chem. A*, 2022, **126**(10), 1591–1604.

51 F. Payton, P. Sandusky and W. L. Alworth, NMR Study of the Solution Structure of Curcumin, *J. Nat. Prod.*, 2007, **70**(2), 143–146.

52 A. Nag, *et al.*, Bent Keto Form of Curcumin, Preferential Stabilization of Enol by Piperine, and Isomers of Curcumin∩Cyclodextrin Complexes: Insights from Ion Mobility Mass Spectrometry, *Anal. Chem.*, 2018, **90**(15), 8776–8784.

53 S. K. Singh and A. Das, The n → π* interaction: a rapidly emerging non-covalent interaction, *Phys. Chem. Chem. Phys.*, 2015, **17**(15), 9596–9612.

54 S. Elnashaie, Z. Chen and P. Prasad, Efficient Production and Economics of Clean-Fuel Hydrogen, *Int. J. Green Energy*, 2007, **4**(3), 249–282.

55 L. A. Alfonso-Herrera, L. M. Torres-Martinez and J. M. Mora-Hernandez, Novel strategies to tailor the photocatalytic activity of metal—organic frameworks for hydrogen generation: a mini-review, *Front. Energy*, 2022, **16**(5), 734–746.

56 E. N. Musa, *et al.*, What Up with MOFs in Photocatalysis (?): Exploring the Influence of Experimental Conditions on the Reproducibility of Hydrogen Evolution Rates, *ACS Appl. Mater. Interfaces*, 2024, **16**(51), 70675–70684.

57 W. Zhang, *et al.*, Optimization of plasmonic metal structures for improving the hydrogen production efficiency of metal-organic frameworks, *Nanoscale*, 2021, **13**(24), 10807–10815.

58 R. Zhang, *et al.*, Post-synthetic platinum complex modification of a triazine based metal organic frameworks for enhanced photocatalytic H2 evolution, *J. Solid State Chem.*, 2019, **271**, 260–265.

59 L.Á. Alfonso Herrera, *et al.*, BDC-Zn MOF sensitization by MO/MB adsorption for photocatalytic hydrogen evolution under solar light, *Mater. Sci. Semicond. Process.*, 2020, **109**, 104950.

60 R. Ren, *et al.*, Exfoliated Molybdenum Disulfide Encapsulated in a Metal Organic Framework for Enhanced Photocatalytic Hydrogen Evolution, *Catalysts*, 2019, **9**(1), 89.

61 H.-Y. Zhang, *et al.*, A new strategy for constructing covalently connected MOF@COF core–shell heterostructures for enhanced photocatalytic hydrogen evolution, *J. Mater. Chem. A*, 2021, **9**(31), 16743–16750.

62 S. Li, *et al.*, Well-distributed Pt-nanoparticles within confined coordination interspaces of self-sensitized porphyrin metal-organic frameworks: synergistic effect boosting highly efficient photocatalytic hydrogen evolution reaction, *Chem. Sci.*, 2019, **10**(45), 10577–10585.

